Research Article | Vol. 29, No. 24 / 22 Nov 2021 / Optics Express 39256

Optics EXPRESS

Sparse-aperture photonics-integrated interferometer (SPIN) imaging system: structural design and imaging quality analysis

TIANBAO CHEN,[1,2] XUEFENG ZENG,[1,4] YINGYING BAI,[1,2] ZHIYU ZHANG,[1,5] YONGJIN WANG,[3] FENG ZHANG,[1] AND XUEJUN ZHANG[1]

[1] *Key Laboratory of Optical System Advanced Manufacturing Technology, Changchun Institute of Optics, Fine Mechanics and Physics, Chinese Academy of Sciences, Changchun, 130033, China*
[2] *University of Chinese Academy of Sciences, Beijing 100049, China*
[3] *Peter Grünberg Research Center, Nanjing University of Posts and Telecommunications, Nanjing, 210003, China*
[4] *zxf@ciomp.ac.cn*
[5] *zhangzhiyu@ciomp.ac.cn*

Abstract: The burgeoning field of astrophotonics, the interface between astronomy and photonics, is redefining astronomical instrumentation to replace traditional bulk optical systems with integrated optics. This drives the development of a new promising photonics-integrated interferometric imaging technique, called the segmented planar imaging detector for electro-optical reconnaissance (SPIDER). Compared to conventional imaging systems, SPIDER can reduce the size, weight, and power (SWaP) by one to two orders of magnitude for an equivalent imaging resolution in virtue of photonics-integrated technology. However, SPIDER has a dense lens distribution and tens of separated narrow wavebands demultiplexed by array waveguide gratings. In this paper, we developed a new simplified sparse-aperture photonics-integrated interferometer (SPIN) imaging system. The SPIN imaging system was no more a Michelson configuration interferometer as SPIDER and was designed as a Fizeau configuration interferometer imaging system. This transfer of configuration type affords a more concise structure; the SPIN was designed with much less apertures and fewer wavebands than those of SPIDER. Further, the SPIN yields enhanced modulation transfer function and imaging quality with equivalent aperture diameter, compared with SPIDER. The main barrier of this transfer is the elimination of coupling restriction at the tip of a waveguide, namely the apodization effect. This effect, which is caused by the coupling effect between Fourier lens and waveguide, hinders SPIN imaging systems from getting finer resolution. However, a microscope could be used to eliminate this effect. Moreover, a waveguide array is used to receive these finer details and enlarges the field of view in SPIN. The coupling efficiency of the waveguides and crosstalk errors between waveguides of array were analyzed, which are important for proper parameters setting in SPIN imaging system. Based on these analyses, the imaging principle was derived and a hyper-Laplacian-based imaging reconstruction algorithm was developed. A simulation of the SPIN imaging system with seven apertures and one imaging waveband demonstrated the high imaging quality.

1. Introduction

Astronomy is an ancient science that has far-reaching and wide-ranging effects on humans. The shadow warriors in the inexorable march of astronomy are telescopes, which capture profound mysteries of the deep universe. Finer observations require high-resolution telescopes. For conventional diffraction-limited optical systems, the resolution is proportional to the primary mirror aperture D. However, the cost increases with at least D^2 or even faster [1–3].

#444421 https://doi.org/10.1364/OE.444421
Journal © 2021 Received 28 Sep 2021; revised 12 Oct 2021; accepted 13 Oct 2021; published 9 Nov 2021

Michelson developed an alternative imaging technology to improve the resolution of the telescope using an optical interferometer and successfully measured the stellar diameter of Betelgeuse [4]. The resolution of the optical interferometer is proportional to the distance, also called the baseline, of two or more light-collecting apertures spaced apart. It is obviously much more economical and easier to increase the baseline than a conventional telescope aperture to acquire a much higher resolution. However, it is challenging to form a fine interferogram [5,6] because unavoidable environmental fluctuations and optical beam manipulations result in high complexity in the optical configuration, which is composed of bulk optical elements with different functions.

To reduce complexity, these bulk optical elements are fully substituted with integrated optics (IO) technology in astrophotonics [7–10]. This technology also spawns a new segmented planar imaging detector for electro-optical reconnaissance (SPIDER) imaging system, which can reduce the size, weight, and power by 10 to 100 times compared with conventional telescopes [11–15]. SPIDER can be classified as a Michelson configuration interferometer [16,17]. The Michelson configuration interferometer uses the pupil-plane beam combination technique to measure complex visibilities in the pupil plane, namely the aperture plane. Measurement with one baseline and one narrow-band wavelength obtains one complex visibility signal. Therefore, SPIDER uses a large number of lenslets, which are used to form baselines, and multiple narrow-band wavelengths [18–20] to measure complex visibilities in the spatial frequency domain [11]. However, owing to the limitation with the distribution of baselines, measurements at high frequency are sparse, which produces Gibbs-ringing artifacts in the reconstructed image [21]. Thus, it is difficult for SPIDER to obtain high-quality imaging performance [13,20,22] at present.

In this study, a new sparse-aperture photonics-integrated interferometer (SPIN) imaging system is proposed, which is designed as a Fizeau configuration interferometer imaging system [16,17]. By introducing IO technology, the SPIN system is compact in structure and stable in measurement. Moreover, a seven-aperture with one narrow waveband SPIN system has been proven to have high imaging quality. In this study, the imaging principle was meticulously derived, which reveals that the SPIN is a Fizeau configuration interferometer imaging system [16,17]. Besides, the apodization effect, which is caused by the coupling effects and hinders the extraction of fine details, has been studied. Therefore, a microscope is added to eliminate this effect. In addition, the relation between the field of view (FOV) and the waveguide array is analyzed after the light is magnified by the microscope. Moreover, the crosstalk between waveguides has been analyzed. The modulation transfer function (MTF) and point spread function (PSF) of SPIN were analyzed. A hyper-Laplacian method has been proposed to reconstruct the ground truth from images obtained in SPIN.

2. Concept of SPIN

The aperture configurations of the conventional monolithic-aperture system, SPIN, and SPIDER are shown in Fig. 1. SPIN was designed as a Fizeau configuration interferometer imaging system. Typically, one narrow waveband and seven apertures can achieve imaging performance similar to the equivalent conventional monolithic-aperture system. This differs significantly from SPIDER, which is a Michelson configuration interferometer and uses a large number of lenslets and multiple narrow-band wavelengths in its system [18–20].

A conceptual diagram of SPIN with two apertures is depicted in Fig. 2. First, the light at the aperture focus is magnified by the microscope and coupled into the waveguide array in the 3D PIC [23]. The optical waveguide is designed as a single-mode waveguide and maintains the same photonic path lengths for the same field of view (FOV) of different apertures. This can reduce the phase shifter's burden of phase adjustment (reducing the optical length difference from the source to the detector to zero) and achieve stable performance in the 3D PIC. Second, the light can be butt-coupled into the subsequent 2D PIC and decomposed into narrow-band

Optics EXPRESS

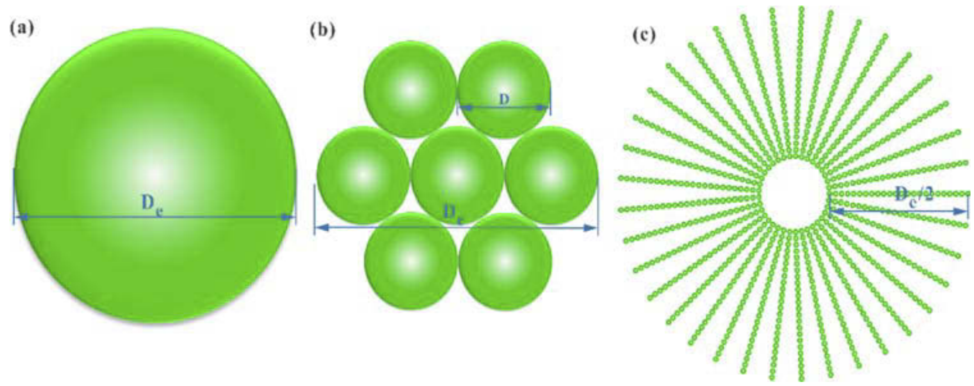

Fig. 1. Aperture configurations of, (a) conventional monolithic aperture system, (b) SPIN, and (c) SPIDER. D_e is the diameter of equivalent conventional monolithic aperture.

light via wavelength-division multiplexing (WDM). Microring resonator-based WDM filters are adopted as demultiplexers, which are compact in size [24,25]. The phase shifter is used for precise cophased adjustment (zero optical length difference from the source to the detector) so that the detector can acquire coherent superposition signals with high contrast. The Y-coupler is used to coherently couple the light from the same FOV of different apertures. The overall conceptual diagram of the 2D PIC is shown in Fig. 2(b). Finally, the interference signals are converted to digital signals by the detector and rearranged to form a degraded image. To analyze the imaging quality, two issues, including the imaging principle and apodization arising from the coupling effect, need to be explored in depth.

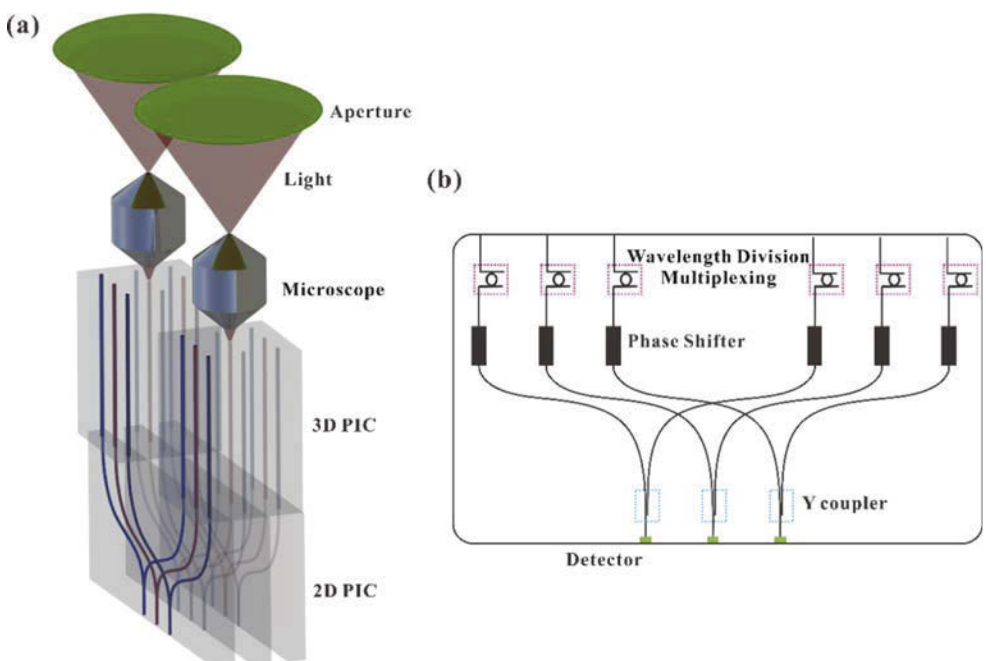

Fig. 2. (a) Conceptual diagram of optical waveguide path layout using 3D PIC and 2D PIC with two apertures in SPIN and (b) functional structure schematic of 2D PIC.

Optics EXPRESS

3. Principle of SPIN

3.1. Imaging principle

Fourier transform apertures are used as light-collecting apertures in SPIN and arranged within a plane to observe the same field. Under these conditions, the overall imaging process was carefully derived (described in the Supplement 1). The signals received by the optical detector are convolution between the target and the PSF of the SPIN system:

$$\mathrm{I}(\vec{\alpha}_1) = \mathrm{I}_0(\vec{\alpha}_1) * \mathrm{PSF}(\vec{\alpha}_1) + n, \tag{1}$$

where n represents the noise introduced by SPIN.

From the aperture function $\mathrm{A}(\vec{\mathrm{R}}) = \mathrm{cir}(2\vec{\mathrm{R}}/\mathrm{D}) * \sum_{\mathrm{i}}^{\mathrm{n}} \delta(\mathrm{R_i})$, the optical transfer function (OTF) and PSF can be derived as

$$\mathrm{OTF}(\vec{R}) = \mathrm{OTF_{cir}}(\vec{R}) * \left[N_T \delta(\vec{R}) + \sum\nolimits_{j>i}^{n} [\delta(\vec{R} - (\vec{R}_j - \vec{R}_i)) + \delta(\vec{R} + (\vec{R}_j - \vec{R}_i))]\right], \tag{2}$$

$$\mathrm{PSF}(\vec{\alpha}_1) = \mathrm{PSF_{cir}}(\vec{\alpha}_1)[N_T + 2 \sum\nolimits_{i<j} \cos(2\pi(\vec{R}_j - \vec{R}_i) \cdot \vec{\alpha}_1)], \tag{3}$$

where $\mathrm{OTF_{cir}}(\vec{R})$ and $\mathrm{PSF_{cir}}(\vec{\alpha}_1)$ are the OTF and PSF of the non-obstructed circular aperture, respectively [26], and N_T is the number of apertures. In contrast to conventional monolithic-aperture imaging systems, the PSF of interferometric imaging systems contains a coherence term owing to the combination of light from different apertures. The coherence terms help to narrow the main lobe of the PSF system and improve the resolution, which will be further discussed in Section 4.2. However, the coupling effect between the single-mode waveguide and the Airy disk couples the entire FOV of $2\lambda/D$ into one waveguide (D is the aperture diameter), which uniformizes fine details within this FOV. The next sections are used to discuss and solve this problem.

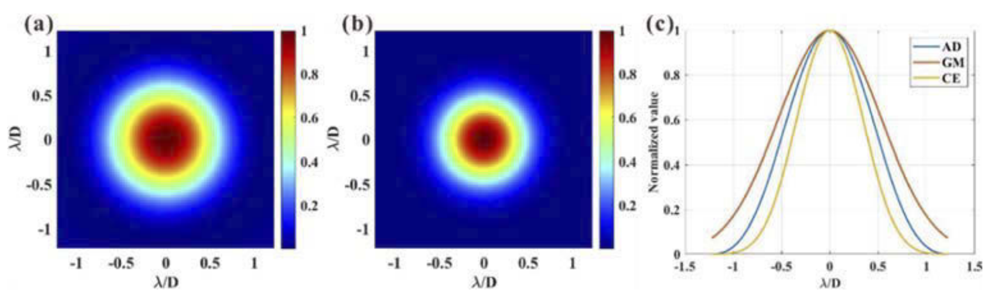

Fig. 3. (a) Distribution of Airy disk within field angle of 2.44λ/D. (b) Distribution of η(α) within field angle of 2.44λ/D, namely the coupling efficiency of intensity. (c) Comparison between Airy disk (AD), Gaussian mode (GD), and η(α) (CE).

3.2. Apodization due to coupling effect

The fraction of light launched into the waveguide/fiber assuming negligible reflections is given by [27–29]

$$\rho = \frac{\left|\int \mathrm{E_{lens}} \mathrm{E}_0^* \mathrm{dS}\right|^2}{\int |\mathrm{E_{lens}}|^2 \mathrm{dS} \times \int |\mathrm{E}_0|^2 \mathrm{dS}}, \tag{4}$$

where $\mathrm{E_{lens}}$ is the electric field distribution in the focal plane of the apertures, $\mathrm{E_0}$ is the propagation mode of the waveguide, and E_0^* represents the complex conjugate of $\mathrm{E_0}$. The gradient of coupling efficiency decreases rapidly with the FOV of the telescope depicted in Fig. 3. With a FOV of λ/D, the gradient of coupling efficiency is 10 times smaller than that on the axis using a single-mode waveguide [27]. Therefore, the FOV of an interferometer that uses one single-mode waveguide per aperture to transport the beam is limited to

$$\mathrm{S} = 2\lambda/D. \tag{5}$$

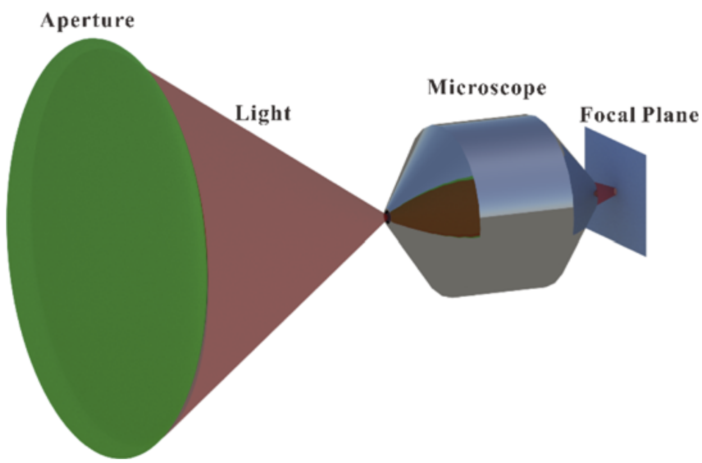

Fig. 4. Diagram of aperture system which magnifies the electric field distribution of the aperture in the focal plane.

The limitation on the coupling efficiency leads to the apodization of the FOV. The apodization effect causes the light within field angle S to be coupled into one waveguide and uniformizes the details finer than the field angle S. To eliminate the apodization effect, a microscope was directly utilized to magnify the spot in the focal plane of each aperture, as depicted in Fig. 4. It is worth mentioning that an improper magnification of the microscope threatens the angular resolution. The angular resolution of two interferometric apertures is λ/B[17], where B is the baseline; therefore, the microscope magnifies the field angle at least by λ/B to $2\lambda/D$. Hence, the magnification of the microscope must be greater than twice the ratio of the maximum baseline B_{max} to D. So far, the apodization effect has been studied. However, the effects introduced by the microscope have not been numerically analyzed, and the relation between the FOV and waveguide array has not been established in SPIN. These are discussed in the following section.

3.3. Relation between FOV and waveguide array in SPIN

The microscope is introduced to acquire finer details than S, which are uniformized by the apodization effect without the microscope. In Eq. (4), ρ is used to illustrate the total fraction of light launched into the waveguide/fiber. However, ρ cannot present the changes of coupling efficiency for arbitrary field angles, which is more appropriate to demonstrate the FOV in SPIN. Thus, the gradient of coupling efficiency η for the arbitrary field angle is used to analyze the ability of the microscope to eliminate the apodization effect. According to the coupling efficiency Eq. (15) in [29], η is the derivative of ρ with respect to S and, with a circular aperture and a fundamental mode approximated by a Gaussian, can be expressed as

$$\eta(r, D, f, \lambda, w) \propto |\mathrm{E}_{\mathrm{lens}}\mathrm{E}_0^*|^2 \propto \left|\frac{J_1(\pi Dr/\lambda f)}{Dr/\lambda f}\exp\left\{-\left(\frac{r}{w}\right)^2\right\}\right|^2, \tag{6}$$

where r is radial coordinate with polar coordinate representation in the focal plane, and f is the focal length of the aperture. w is the 1/e width of the Gaussian mode and can be expressed as

$$w = \mathrm{a}_r\left(0.65 + \frac{1.619}{V^{3/2}} + \frac{2.879}{V^6}\right), \tag{7}$$

Herein, V is normalized frequency, and cutoff occurs as $V \leq 2.4$ for single-mode waveguide/fiber [29]. a_r is the core radius/length of the waveguide/fiber. The arbitrary field angle, observed by SPIN, is $\alpha = r/f$, so the $\eta(\alpha)$ can be expressed as

$$\eta(\alpha) = \mathrm{C_N}\left|\frac{\mathrm{J}_1(\pi D\alpha/\lambda)}{D\alpha/\lambda}\exp\left\{-\left(\frac{\alpha}{w}f\right)^2\right\}\right|^2, \tag{8}$$

where $\mathrm{C_N}$ is the constant for normalization. To demonstrate the apodization effect, a simulation with $\mathrm{a}_r = 3\mu\mathrm{m}$ and $V = 2.4$, is implemented in Fig. 3.

The coupling efficiency is related to a_r, and $\sqrt{\eta(\alpha=0)} \cong 0.1\sqrt{\eta(\alpha=0)}$ with $\mathrm{a}_r = 4\mu\mathrm{m}$, which has been reported in [27,28]. This means that the field angle of $2\lambda/D$ only couples into one waveguide. To eliminate this effect and detect finer interferometric details, the microscope and the waveguide array are adopted. To better model the relation between the FOV and waveguide array, $\eta(\alpha)$, with the microscope and waveguide array adopted in SPIN, is simulated as shown in Fig. 5.

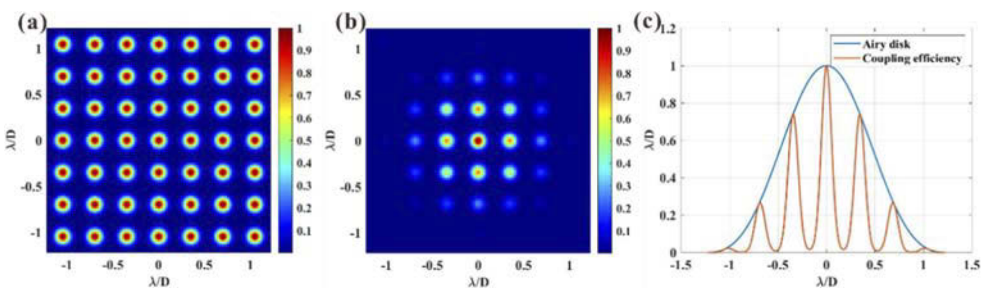

Fig. 5. (a) Gaussian mode distribution of 7 * 7 waveguide with magnification $\beta = 10$. (b) Distribution of $\eta(\alpha/\beta)$. (c) Profile of the magnified Airy disk and $\eta(\alpha/\beta)$. Note: the coordinate of the field angle is the observed field of view, not the coordinate of the magnified field in the focal plane.

The coupling efficiency with the microscope and waveguide array within the FOV of S has been demonstrated, and the apodization effect has been solved, as shown in Fig. 5. The finer detail within S can be received. The duty cycle d, which is the ratio of the waveguide diameter to distance between adjacent waveguides, is slightly larger than 0.5 in the simulation. The parameters of the aperture configurations are depicted in Fig. 1(b). The field angle of adjacent waveguides is $\frac{2.44\lambda}{7\mathrm{D}}$, and the maximum angular resolution of SPIN is $\frac{\lambda}{\mathrm{B_{max}}} = \frac{\lambda}{2\mathrm{D}}$. Thus, the waveguide array and magnification settings are sufficient for observations, and the FOV in horizontal/vertical direction is $\frac{2.44\lambda}{7\mathrm{D}} * N_w$ (where N_w is the waveguide number in the horizontal/vertical direction). However, owing to the coupled-mode theory, crosstalks between waveguides could affect the intensity received by individual detectors, which will be analyzed in the next section.

3.4. Crosstalk error in waveguide array

The coupled-mode theory reveals that the power of adjacent waveguides transfers between each other. Fortunately, this transfer is spatially periodic. Thus, a certain length of the waveguide can reduce or even avoid this transfer, which introduces errors to the interferometric pattern.

Optics EXPRESS

According to [30], the complex amplitudes of adjacent waveguides are $A(z)$ and $B(z)$. If the boundary conditions are such that a single mode, say $B(z)$, is incident at $z = 0$ on the perturbed region $z>0$, the boundary conditions can be expressed as

$$B(0) = B_0, A(0) = 0 \tag{9}$$

Then, the $A(z)$ and $B(z)$ can be expressed as [30]

$$A(z) = B_0 \frac{2\kappa}{(4\kappa^2 + \Delta^2)^{1/2}} e^{-iz\Delta/2} \sin\left[\frac{1}{2}(4\kappa^2 + \Delta^2)^{1/2} z\right], \tag{10}$$

$$B(z) = B_0 e^{-iz\Delta/2} \left\{\cos\left[\frac{1}{2}(4\kappa^2 + \Delta^2)^{1/2} z\right] - i\frac{\Delta}{(4\kappa^2 + \Delta^2)^{1/2}} \sin\left[\frac{1}{2}(4\kappa^2 + \Delta^2)^{1/2} z\right]\right\} \tag{11}$$

where Δ is a phase-mismatch constant and depends on the propagation constants (β_a and β_b) of two waveguides. In the SPIN system, the array of waveguides has the same design, so Δ equals zeros. Thus, under phase-matched condition $\Delta = 0$, a complete spatially periodic power transfer between two waveguides occurs with a period $\pi/2\kappa$:

$$A(z) = B_0 \sin(\kappa z), \tag{12}$$

$$B(z) = B_0 \cos(\kappa z) \tag{13}$$

Hence, an appropriate length of the straight waveguide in 3D PIC can prevent crosstalks between waveguides. The distance can be set as $\mathrm{M}\pi/\kappa$, $(\mathrm{M} = 1, 2, 3, \ldots)$, where κ is the coupling coefficient [31] and can be expressed as

$$\kappa = \frac{2p_x^2 k_x^2}{\beta(p_x^2 + k_x^2)(1 + \mathrm{a}_r p_x)} \exp(-p_x d) \tag{14}$$

Here,

$$k_x \mathrm{a}_r = m\pi - 2\arctan\left(\frac{k_x}{p_x}\right), (m = 0, 1, 2, \ldots), \tag{15}$$

$$k_y \mathrm{a}_r = n\pi - 2\arctan\left(\frac{n_2^2 k_y}{n_1^2 p_y}\right), (n = 0, 1, 2, \ldots), \tag{16}$$

$$\beta = (k_0^2 n_1^2 - k_x^2 - k_y^2)^{1/2}, \tag{17}$$

$$p_x = (k_0^2 n_1^2 - k_0^2 n_2^2 - k_x^2)^{1/2}, \tag{18}$$

$$p_y = (k_0^2 n_1^2 - k_0^2 n_2^2 - k_y^2)^{1/2}, \tag{19}$$

where, n_1 and n_2 are the refractive index of core and cladding in the waveguide, respectively, $k_0 = \frac{2\pi}{\lambda}$, d is the distance between adjacent waveguides.

4. Analysis of SPIN imaging system

4.1. MTF

In imaging systems, the MTF characterizes the contrast changes of different spatial frequencies [32] and the finest resolution. Hence, MTF is used to analyze imaging performance and is adopted to compare the contrast changes of the conventional monolithic aperture, SPIN, and SPIDER systems, as shown in Fig. 1.

Optics EXPRESS

SPIDER interferes with the light of the pupil plane and measures the complex visibility of the targets [28]. The complex visibility is the Fourier transform of the targets with a fixed spatial frequency $\vec{f} = \vec{B}/(\lambda z_0)$:

$$V(\vec{f}) = \int I_0(\vec{x})\exp(-i2\pi\vec{f}\cdot\vec{x})d\vec{x}\Big|_{\vec{f}=\vec{B}/(\lambda z_0)} \tag{20}$$

Hence, the MTF equals 1 when the corresponding spatial frequency is measured and 0 otherwise. The SPIDER measurements have a separate radial distribution. Therefore, the visibility measurements in some radial directions are unavoidably missed, as depicted in Fig. 6 and the blue line in Figs. 6(d) and 6(e). Conversely, SPIN can maintain almost the same contrast response in different directions and guarantee that all spatial frequency signals under $D_e/\lambda z$ are measured with aperture configuration depicted in Fig. 1(b), as shown in Fig. 6(a) and the red lines in Figs. 6(d) and 6(e).

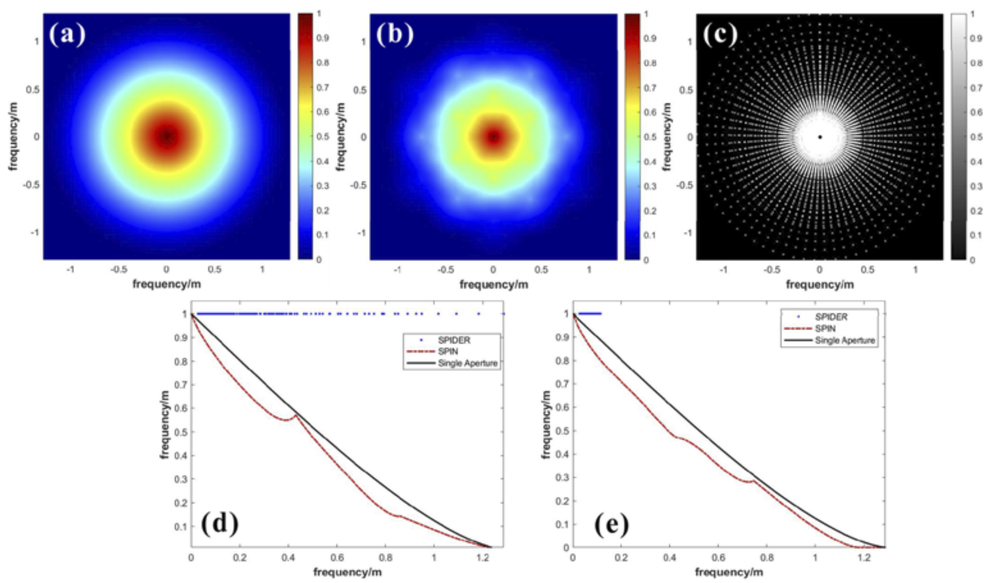

Fig. 6. MTF of (a) conventional monolithic aperture, (b) SPIN, and (c) SPIDER systems with aperture configurations depicted in Fig. 1, which have the same aperture diameter. (d) Horizontal MTF distribution and (e) vertical MTF distribution.

The MTF of SPIN is more suitable for low-frequency intensive observations [21,33], which is the characteristic of real-world images and shows a heavy-tailed distribution of gradients [34–36]. However, the MTF of SPIDER displays a lower performance for a heavy-tailed distribution of gradients than when using the salient features with significant gradient changes [20]. Moreover, a zero weight in MTF, namely spectrum leakage, results in Gibbs ringing artifacts in images [21,37], which has been demonstrated in the Supplement 1. In addition, the measurements of complex visibilities are sparse at present [15,19] in SPIDER. Hence, more complicated priors and algorithms are required to reconstruct high-quality images in SPIDER [15,18].

4.2. Aperture configurations and PSFs

A seven-aperture configuration was chosen for SPIN. Fewer apertures can be arranged, as shown in Figs. 7(b) and 7(c). Apart from the number of apertures, their arrangement must also be carefully selected. The PSF is chosen to characterize these variables, which represent the system

Optics EXPRESS

response for the point source. The PSF of the system can be expressed by Eq. (3) as

$$\mathrm{PSF}(\vec{\alpha}_1) = \mathrm{PSF}_{\mathrm{cir}}(\vec{\alpha}_1)\left[N_T + 2\sum\nolimits_{i<j}\cos(2\pi(\vec{R}_j - \vec{R}_i)\cdot\vec{\alpha}_1)\right]. \tag{21}$$

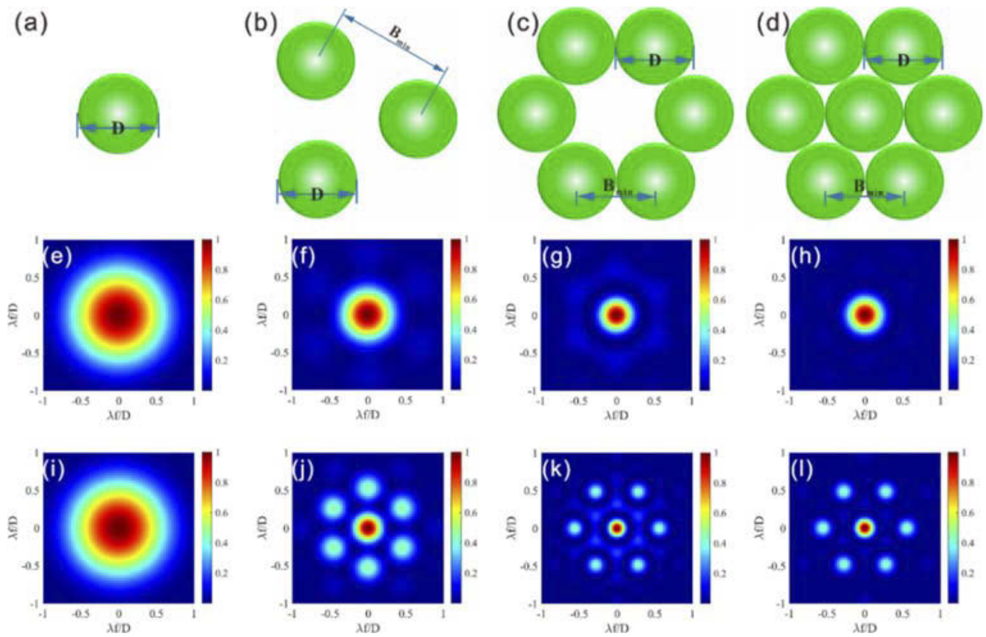

Fig. 7. Configurations of (a) sub-aperture, (b) three apertures, (c) six apertures, and (d) seven apertures in the first row. The PSFs of the configurations with $B_{min} = D$ are shown by (e), (f), (g), and (h). The PSFs of the configurations with $B_{min} = 2D$ are shown by (i), (j), (k), and (l).

The cosine terms can narrow $\mathrm{PSF}_{\mathrm{cir}}$, which is the PSF of a sub-aperture, as shown in Fig. 7(e). However, these terms cannot entirely narrow the overall PSF to a smaller value. In addition, the sidelobes in PSF vary with the number and arrangement of apertures, and a simulation of three different configurations was implemented to address the influence. The uniform arrangements of the three -, six -, and seven-aperture configurations are shown in Figs. 7(b), 7(c), and 7(d), respectively. The PSFs of these configurations with a minimum spacing $B_{min} = D$ and $B_{min} = 2D$ are shown in the second and last rows of Fig. 7, respectively.

At the same equivalent aperture, more apertures result in fewer sidelobes in the PSF and a similar width of the main lobe (configurations (b) and (c) in Fig. 7). A large spacing of adjacent apertures can narrow the main lobe; however, it causes evident sidelobes. To acquire a high resolution, a large spacing with $B_{min} = 2D$ is adopted in the SPIN imaging system. Moreover, a deconvolution image reconstruction model is proposed to remove the degradation introduced by the sidelobes.

5. SPIN performance in simulation

5.1. Image reconstruction model

According to the principle of SPIN, the imaging model can be expressed as

$$I = X * K + n, \tag{22}$$

where I represents the degraded images received by the system, X is the ground truth of the observations, and K is the PSF of the imaging system. In actual measurements, noise n is introduced by a photoelectric detector, environmental fluctuations, and other errors.

SPIN concentrates on natural scenes, which are heavy-tailed distributions of gradients [34], and hyper-Laplacian (HL i.e., $p(x) \propto e^{-k|x|^{\alpha}}$) can measure these distributions well [35,36]. Hence, the HL prior was added to the reconstruction. From a probabilistic perspective, the reconstruction seeks a maximum a posteriori (MAP) estimation of x satisfying: $p(x|I, K) \propto p(I|x, K)p(x)$. The first term is a Gaussian likelihood, and the second term is the HL prior:

$$\begin{aligned} p(I|x, K) &\propto \exp\left\{-\sum_i^N \frac{\eta}{2}(x*K-I)_i^2\right\}, \\ p(x) &\propto \exp\left\{-\sum_i^N \sum_j^J |(x*f_j)_i|^{\alpha}\right\}, \end{aligned} \tag{23}$$

where i is the pixel index, x is the estimation of the ground truth X, and $f_1, \ldots f_J$ represent a set of filters applied to x. To obtain the MAP estimation, the probability distribution $p(x|I, K)$ needs to be maximized, which equivalently minimizes, $-\log[p(I|x, K)p(x)]$, yielding the following reconstruction model:

$$\min_x \sum_i^N \left(\frac{\eta}{2}(x*K-I)_i^2 + \sum_j^J |(x*f_j)_i|^{\alpha}\right). \tag{24}$$

The HL prior can precisely model the distribution of image gradients; hence, this filter is set to calculate the image gradients. The first-order derivative operators are $f_1 = [1, -1]$ and $f_2 = [1, -1]^T$ for the horizontal and vertical directions of the image gradients, respectively [38]. For simplicity, the HL prior is denoted $F_i^j x \equiv (x*f_j)_i$ as $j = 1 \ldots J$.

To move the $F_i^j x$ term out of $|.|^{\alpha}$ expression, the half-quadratic penalty method [39,40] is used in the reconstruction model and two auxiliary variables u_i, v_i are introduced at pixel i:

$$\min_{x,u,v} \sum_i \left(\frac{\eta}{2}(x*K-I)_i^2 + \frac{\beta}{2}(||F_i^1 x - u_i||_2^2 + ||F_i^2 x - v_i||_2^2) + |u_i|^{\alpha} + |v_i|^{\alpha}\right). \tag{25}$$

It is difficult to solve the half-quadratic penalty problem directly. Alternatively, the original problem can be divided into two sub-problems which can be solved separately:

$$x^{n+1} = \arg\min_x \sum_i \left(\frac{\eta}{2}||x*K-I||_2^2 + \frac{\beta}{2}(||F^1 x - u||_2^2 + ||F^2 x - v||_2^2)\right), \tag{26}$$

$$u^{n+1} = \arg\min_u \sum_i \left(\frac{\beta}{2}||F^1 x - u||_2^2 + |u|^{\alpha}\right), \tag{27}$$

$$v^{n+1} = \arg\min_v \sum_i \left(\frac{\beta}{2}||F^2 x - v||_2^2 + |v|^{\alpha}\right). \tag{28}$$

(1) x sub-problem

Differentiating with respect to x, the resulting derivative is

$$\left(F^{1^T}F^1 + F^{2^T}F^2 + \frac{\eta}{\beta}k^T k\right)x = F^{1^T}u + F^{2^T}v + \frac{\eta}{\beta}k^T \mathrm{I}, \tag{29}$$

where $kx = x*K$. The convolution matrices F^1, F^2 and k can be diagonalized using a 2D FFT with circular boundary conditions. Hence, the optimal x is expressed as

$$x^{n+1} = \mathcal{F}^{-1}\left(\frac{\mathcal{F}(F^{1^T}).\times\mathcal{F}(u) + \mathcal{F}(F^{2^T}).\times\mathcal{F}(v) + (\eta/\beta)\mathcal{F}(k^T).\times\mathcal{F}(\mathrm{I})}{\mathcal{F}(F^{1^T}).\times\mathcal{F}(F^1) + \mathcal{F}(F^{2^T}).\times\mathcal{F}(F^2) + (\eta/\beta)\mathcal{F}(k^T).\times\mathcal{F}(k)}\right), \tag{30}$$

where $.\times$ denotes component-wise multiplication, namely, the Hadamard product. $\mathcal{F}$ and $\mathcal{F}^{-1}$ respectively represent Fourier transform and inverse Fourier transform. The division is also component-wise.

(2) u, v sub-problem

Given the solution of x^{n+1}, u and v satisfy:

$$\alpha|u|^{\alpha-1}sign(u) + \beta(u - F^1 x^{n+1}) = 0, \tag{31}$$

$$\alpha|v|^{\alpha-1}sign(v) + \beta(v - F^2 x^{n+1}) = 0, \tag{32}$$

where $u, v \neq 0$. For $\alpha = 1/2$ and $\alpha = 2/3$, sub-problem (2) has an analytic solution, and a lookup table (LUT) is established, which can solve sub-problems quickly and accurately compared with a numerical root-finder [35].

(3) Termination Conditions

$$\beta \geq \beta_{max} \tag{33}$$

Starting with a small value β_0, β^{n+1} is scaled by a factor β_{amp} until it exceeds the fixed value β_{max}. When minimizing the reconstruction model in Eq. (25), the two sub-problems are alternately solved for $M(M \geq 1)$ times, before increasing β. The initialization technology and the choice of the coefficients have been discussed in [35].

5.2. Imaging simulation

The PSF of the interferometer with N_T apertures can be expressed as:

$$\mathrm{PSF}(\vec{\alpha}) = \mathrm{PSF}_{\mathrm{cir}}(\vec{\alpha})\left[N_T + \sum_{j=1}^{N_B} 2\cos\left(\frac{2\pi}{\lambda}\vec{B}_j \cdot \vec{\alpha}\right)\right] \tag{34}$$

where $\mathrm{PSF}(\vec{\alpha})$ is the PSF of a sub-aperture, and N_B is the number of baselines with $N_B = N_T(N_T - 1)/2$, provided the distribution of the telescopes is non-redundant.

The minimum baseline is twice that of a sub-aperture used to obtain a narrow mainlobe of the PSF and a higher resolution. The microscope magnification is set similarly to the parameters simulated in Section 3.3. We demonstrated the feasibility of SPIN with a seven-aperture configuration. The structural parameters of the simulated system are listed in Table 1, and the PSF is shown in Fig. 8.

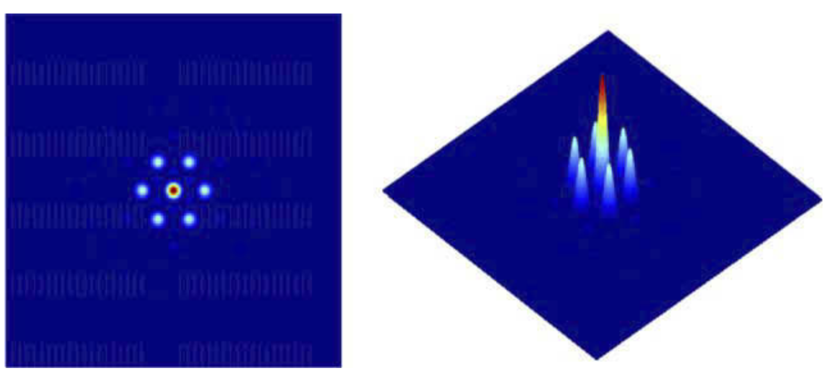

Fig. 8. PSF of seven-apertures array configuration.

The similarity between the reconstructed object distribution and ground truth is further evaluated using the peak signal-to-noise ratio (PSNR), structural similarity index (SSIM), and signal-to-noise ratio (SNR) [41]. The test dataset includes images that are widely used for image restoration validation [42]. Some of these images are shown in Fig. 9.

Optics EXPRESS

Table 1. Design structural parameters of the system.

Structure Parameters	Value
Magnification of the microscope	15
Waveguide arrays behind the aperture system	512 × 512
Aperture diameter	30 mm
Aperture focal length	60 mm
Number of apertures	7
Minimum baseline	60 mm
Wavelength	1550 nm

Fig. 9. Some of the widely used testing images in image reconstruction.

Table 2. Peak signal-to-noise ratio and structural similarity index of the reconstruction.

Images \ Methods	SNR(dB)	Boats	Butterfly	Zebra	Pyramid	Cameraman
Degraded	30	27.40/0.67	29.04/0.58	27.40/0.67	27.71/0.65	28.63/0.62
	20	19.80/0.28	20.17/0.22	19.73/0.30	19.83/0.25	20.19/0.23
HL method	30	**29.07/0.78**	**34.84/0.92**	**31.23/0.86**	**28.74/0.79**	**33.56/0.90**
	20	**27.89/0.72**	**31.74/0.87**	**29.02/0.81**	**28.58/0.75**	**30.93/0.81**

In the Supplement 1, comparison between SPIN and Fizeau interferometer reveals that the SNR of SPIN would be lower than that of the Fizeau interferometer. Therefore, two lower SNR cases of 20dB and 30dB, which are typically set as 30dB and 40dB Gaussian noise for Fizeau interferometer [43], are simulated with the block-matching and 3D filtering (BM3D) denoising algorithm [44]. The received images are preprocessed by the BM3D denoising algorithm. Subsequently, the preprocessed images are reconstructed by the HL method. Table 2 lists the degraded and reconstructed assessments of the test images with Gaussian white noise with zero mean and variance of 0.01 and 0.001 corresponding to SNR of 20dB and 30dB, and two visual illustrations are provided in Fig. 10 and Fig. 11. These assessments and visual illustrations showed excellent imaging quality using the SPIN and HL methods. For better comparison of imaging quality, a simple simulation of the same target with SPIDER and SPIN system is demonstrated in the Supplement 1. Moreover, our previous work showed the imaging quality using resolution board (USAF1951) targets of SPIDER system [21]; similar results were reported elsewhere [19,20]. These comparisons show that the SPIN has superior imaging quality for natural scenes, which are heavy-tailed distributions of gradients.

To expand field of use with SPIN, especially for some astronomical applications, which do not conform to the heavy-tailed distributions of gradients in large extent, a simple discussion is presented in the Supplement 1. This discussion encourages that a more appropriate prior and method are needed in the SPIN system for special applications. In addition, a fine optimization for suppressing noise is needed in the SPIN system.

Optics EXPRESS

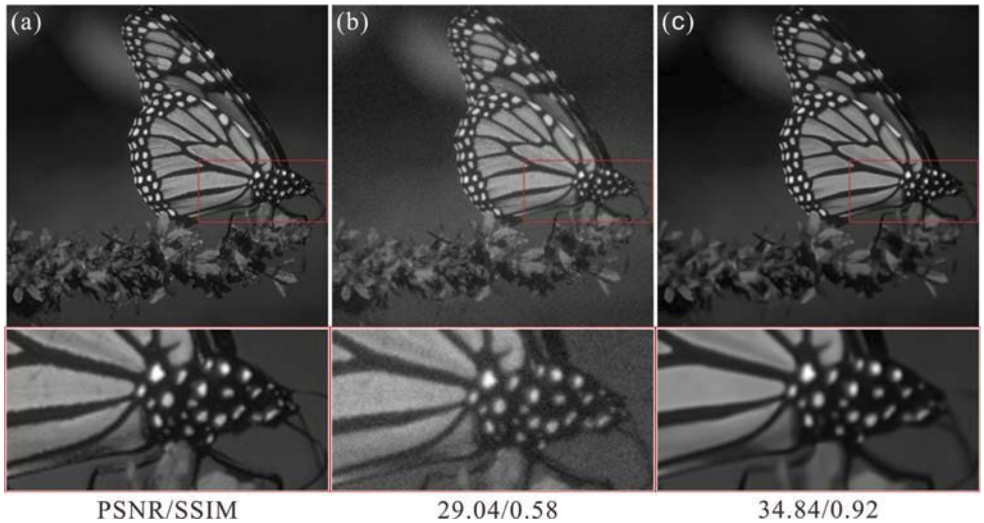

Fig. 10. Illustration of the results of the final reconstructed image when the SNR is 30dB. (a) Original clear image. (b) Degraded image. (c) Result obtained by the HL method.

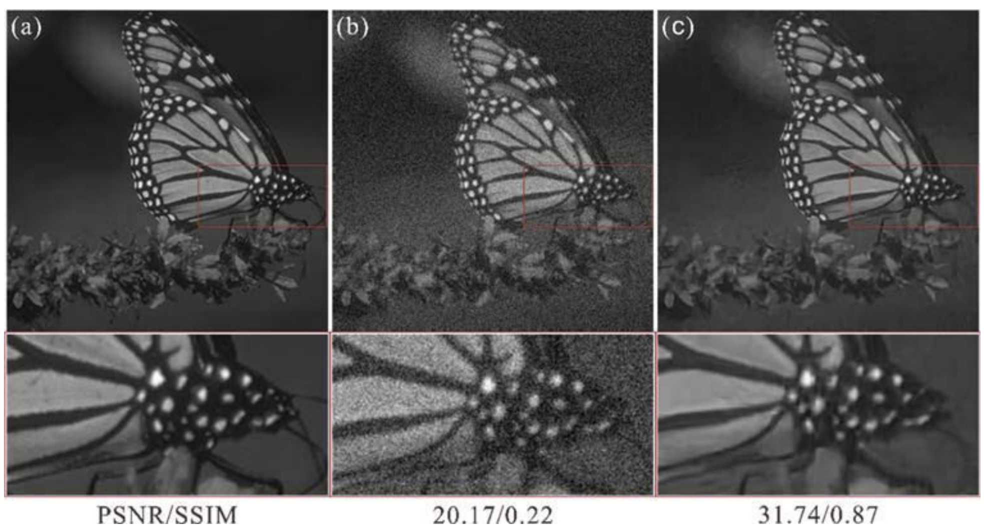

Fig. 11. Illustration of the results of the final reconstructed image when the SNR is 20dB. (a) Original clear image. (b) Degraded image. (c) Result obtained by the HL method.

Optics EXPRESS

6. Conclusion

In this paper, we propose SPIN, which is a compact interferometric imaging system based on an advanced photonics technique. It was demonstrated that SPIN has high-quality imaging performance with a seven-aperture configuration and one imaging waveband. Therefore, SPIN can significantly reduce the number of apertures and the number of imaging wavebands. The MTF analysis shows that SPIN can obtain a more uniform response in the spatial frequency domain and receive most spatial frequency signals within the diffraction limit. Hence, SPIN makes it easier to reconstruct high-quality images.

Funding. National Natural Science Foundation of China (61975201); Youth Innovation Promotion Association of the Chinese Academy of Sciences; Advanced Science Key Research Project, Chinese Academy of Science (QYZDJ-SSW-JSC038); Key Foreign Cooperation Projects of International Cooperation Bureau, Chinese Academy of Science (181722KYSB20180015).

Acknowledgment. The authors would like to thank the anonymous referees for their valuable suggestions and comments that have helped improve the paper.

Disclosures. The authors declare no conflicts of interest.

Data availability. Data underlying the results presented in this paper are not publicly available at this time but may be obtained from the authors upon reasonable request.

Supplemental document. See Supplement 1 for supporting content.

References

1. N. Blind, E. L. Coarer, P. Kern, and S. Gousset, "Spectrographs for astrophotonics," Opt. Express **25**(22), 27341–27369 (2017).
2. A. B. Meinel, "Cost relationships for nonconventional telescope structural configurations," J. Opt. Soc. Am. **72**(1), 14–20 (1982).
3. H.P. Stahl, A.F. Prince, C. Smart, K. Stephens, and T. Henrichs, "Preliminary cost model for space telescopes,", in *Proceedings of UV/Optical/IR Space Telescopes: Innovative Technologies and Concepts IV* 7436, 743602 (2009).
4. A. A. Michelson and F. G. Pease, "Measurement of the diameter of Alpha-Orionis by the interferometer," Astrophys. J. **53**, 249–259 (1921).
5. J. Bland-Hawthorn and P. Kern, "Astrophotonics: a new era for astronomical instruments," Opt. Express **17**(3), 1880–1884 (2009).
6. A. Labeyrie, S. G. Lipson, and P. Nisenson, *An introduction to optical stellar interferometry* (Cambridge University, 2006).
7. C. Cunningham, "Future optical technologies for telescopes," Nat. Photonics **3**(5), 239–241 (2009).
8. J. Bland-Hawthorn and G. L. Sergio, "Astrophotonics: molding the flow of light in astronomical instruments," Opt. Express **25**(13), 15549–15557 (2017).
9. J. Bland-Hawthorn, "Astrophotonics: the future of astronomical instrumentation," *CLEO: 2015, OSA Technical Digest (online)* (Optical Society of America, 2015), p. STu4L.1.
10. P. Kern, J. P. Berger, P. Haguenauer, F. Malbet, and K. Perraut, "Planar Integrated Optics and astronomical interferometry," Comptes Rendus de l'Académie des Sciences - Series IV - Physics **2**(1), 111–124 (2001).
11. R.L. Kendrick, A. Duncan, C. Ogden, J. Wilm, D.M. Stubbs, S.T. Thurman, T. Su, R.P. Scott, and S.J. Yoo, "Flat-panel space-based space surveillance sensor," in *Proceedings of the Advanced Maui Optical and Space Surveillance Technologies Conference*, 2013.
12. T. Su, R. P. Scott, C. Ogden, S. T. Thurman, R. L. Kendrick, A. Duncan, R. Yu, and S. J. Yoo, "Experimental demonstration of interferometric imaging using photonic integrated circuits," Opt. Express **25**(11), 12653–12665 (2017).
13. T. Su, G. Liu, K. E. Badham, S. T. Thurman, R. L. Kendrick, A. Duncan, D. Wuchenich, C. Ogden, G. Chriqui, S. Feng, and J. Chun, "Interferometric imaging using Si3N4 photonic integrated circuits for a SPIDER imager," Opt. Express **26**(10), 12801–12812 (2018).
14. A. Duncan, R. Kendrick, C. Ogden, D. Wuchenich, S. Thurman, T. Su, W. Lai, J. Chun, S. Li, G. Liu, and S.J. Yoo, "SPIDER: next generation chip scale imaging sensor," In *Proceedings of the Advanced Maui Optical and Space Surveillance Technologies Conference*, 2014.
15. L. Pratley and J.D. McEwen, "Sparse image reconstruction for the SPIDER optical interferometric telescope," in *Proceedings of the 9th International Conference on Photonics*, Optics and Laser Technology, 2019.
16. Q. Yu, B. Ge, Y. Li, Y. Yue, F. Chen, and S. Sun, "System design for a "checkerboard" imager," Appl. Opt. **57**(35), 10218–10223 (2018).
17. W. P. Gao, X. R. Wang, L. Ma, Y. Yuan, and D. F. Guo, "Quantitative analysis of segmented planar imaging quality based on hierarchical multistage sampling lens array," Opt. Express **27**(6), 7955–7967 (2019).

Optics EXPRESS

18. C. Ding, X. Zhang, X. Liu, H. Meng, and M. Xu, "Structure Design and Image Reconstruction of Hexagonal-Array Photonics Integrated Interference Imaging System," IEEE Access **8**, 139396–139403 (2020).
19. T. Chen, X. Zeng, Z. Zhang, F. Zhang, Y. Bai, and X. Zhang, "REM: A simplified revised entropy image reconstruction for photonics integrated interference imaging system," Opt. Commun. **501**, 127341 (2021).
20. E. J. Candès and M. B. Wakin, "An introduction to compressive sampling," IEEE Signal Process. Mag. **25**(2), 21–30 (2008).
21. J.D. Monnier, "Optical interferometry in astronomy," in Reports on Progress in Physics **66**(5), 789 (2003).
22. A. Glindemann, *Principles of stellar interferometry* (Springer, 2011.).
23. S. B. Yoo, B. Guan, and R. P. Scott, "Heterogeneous 2D/3D photonic integrated microsystems," Microsyst. Nanoeng. **2**(1), 16030 (2016).
24. X. Zheng, I. Shubin, G. Li, T. Pinguet, A. Mekis, J. Yao, H. Thacker, Y. Luo, J. Costa, K. Raj, and J.E. Cunningham, "A tunable 1×4 silicon CMOS photonic wavelength multiplexer/demultiplexer for dense optical interconnects," Opt. Express **18**(5), 5151–5160 (2010).
25. B. E. Little, S. T. Chu, H. A. Haus, J. Foresi, and J. Laine, "Micro-ring resonator channel dropping filters," J. Lightwave Technol. **15**(6), 998–1005 (1997).
26. J.W. Goodman, *Introduction to Fourier Optics Fourth edition* (W. H. Freeman and Company, 2005).
27. O. Guyon, "Wide field interferometric imaging with single-mode fibers," Astron. Astrophys. **387**(1), 366–378 (2002).
28. Q. Yu, D. Wu, F. Chen, and S. Sun, "Design of a wide-field target detection and tracking system using the segmented planar imaging detector for electro-optical reconnaissance," Chin. Opt. Lett. **16**(7), 071101 (2018).
29. S. Shaklan and F. Roddier, "Coupling starlight into single-mode fiber optics," Appl. Opt. **27**(11), 2334–2338 (1988).
30. A. Yariv, "Coupled-mode theory for guided-wave optics," IEEE J. Quantum Electron. **9**(9), 919–933 (1973).
31. E. A. Marcatili, "Dielectric rectangular waveguide and directional coupler for integrated optics," Bell Labs Tech. J. **48**(7), 2071–2102 (1969).
32. VN Mahajan, *Optical Imaging and Aberrations: Part II: Wave Diffraction Optics: Second Edition* (SPIE, 2001).
33. Q. Chu, Y. Shen, M. Yuan, and M. Gong, "Numerical simulation and optimal design of segmented planar imaging detector for electro-optical reconnaissance," Opt. Commun. **405**(15), 288–296 (2017).
34. E.P. Simoncelli, "Bayesian denoising of visual images in the wavelet domain," *Bayesian inference in wavelet-based models*. Springer: New York (1999), pp. 291–308.
35. D. Krishnan and R. Fergus, "Fast image deconvolution using hyper-Laplacian priors," presented at Neural Information Processing Systems, Vancouver, Canada, 3 Dec. 2009.
36. E.P. Simoncelli and E.H. Adelson, "Noise removal via Bayesian wavelet coring," in *Proceedings of IEEE Conference on Image Processing* (IEEE, 1996), pp. 379–382.
37. J. Veraart, E. Fieremans, I. O. Jelescu, F. Knoll, and D. S. Novikov, "Gibbs ringing in diffusion MRI," Magn. Reson. Med. **76**(1), 301–314 (2016).
38. W. Lu, J. Duan, Z. Qiu, Z. Pan, R. Liu, and L. Bai, "Implementation of high-order variational models made easy for image processing," Math. Meth. Appl. Sci. **39**(14), 4208–4233 (2016).
39. D. Geman and C. Yang, "Nonlinear image recovery with half-quadratic regularization," IEEE Trans. on Image Process. **4**(7), 932–946 (1995).
40. Y. Wang, J. Yang, W. Yin, and Y. Zhang, "A new alternating minimization algorithm for total variation image reconstruction," SIAM J. Imaging Sci. **1**(3), 248–272 (2008).
41. Z. Wang, A. C. Bovik, H. R. Sheikh, and E. P. Simoncelli, "Image quality assessment: from error visibility to structural similarity," IEEE Trans. on Image Process. **13**(4), 600–612 (2004).
42. K. Zhang, W. Zuo, Y. Chen, D. Meng, and L. Zhang, "Beyond a gaussian denoiser: Residual learning of deep CNN for image denoising," IEEE Trans. on Image Process. **26**(7), 3142–3155 (2017).
43. M. Hui, Y. Wu, W. Li, M. Liu, L. Dong, L. Kong, and Y. Zhao, "Image restoration for synthetic aperture systems with a non-blind deconvolution algorithm via a deep convolutional neural network," Opt. Express **28**(7), 9929–9943 (2020).
44. K. Dabov, A. Foi, V. Katkovnik, and K. Egiazarian, "Image Denoising by Sparse 3-D Transform-Domain Collaborative Filtering," IEEE Trans. on Image Process. **16**(8), 2080–2095 (2007).